

Long-term wind and wave energy resource assessment in the South China sea based on 30-year hindcast data

Zhifeng Wang^{a,b}, Chenglin Duan^{a,b}, Sheng Dong^{a,b,*}

^a College of Engineering, Ocean University of China, Qingdao 266100, China

^b Shandong Province Key Laboratory of Ocean Engineering, Ocean University of China, Qingdao 266100, China

ARTICLE INFO

Keywords:

Wind energy
Wave energy
Numerical modelling
South China sea

ABSTRACT

The long-term wind and wave characteristics, and their associated stored power, are investigated in the South China Sea (SCS) from 1986 to 2015. The Weather Research and Forecasting model (WRF) and WAVEWATCH-III (WW III) are continuously performed to simulate a 30-year wind and wave hindcasts in the entire domain. Comparisons between the simulated and observed wind and wave data show good agreement under extreme typhoon conditions as well. The spatio-temporal patterns of annual, seasonal and monthly averaged wind fields and wind power density, significant wave heights, and wave potential are presented using the 30-year simulated results. Our results show that offshore winds and waves, with mean annual energy densities reaching up to 1100 W/m^2 and 65 kW/m , respectively, are relatively stronger than they are nearshore or inland. The most abundant power occurs in December and the least abundant appears in May. Furthermore, wind and wave energy roses of average power potential at 15 typical points across the SCS are calculated at length. The dominant directions for both the wind and waves are consistently NNE, NE, and ENE. Additionally, the wave energy is mainly the result of energy periods (between 6 and 11 s) and significant wave heights (between 1 and 6 m).

1. Introduction

As a result of climate warming, the limited storage of fossil fuels and the continuous soaring oil expenses, the development of renewable energy becomes more and more important than before. Many alternatives, such as solar, wind and ocean energy, can be selected in the future (Ueckerdt et al., 2015). Wind and wave energy are enormous sources of renewable energy, due to their limited negative environmental impacts. Previous valuation of wind and wave energy potential so far have been conducted, based on reanalysis datasets and numerical models, at a global scale (e.g., Arinaga and Cheung, 2012; Zheng and Pan, 2014) or across various regions (e.g., Kamranzad et al., 2013; Akpinar et al., 2016). Meanwhile, offshore wave energy converters and wind turbines are being continually designed and optimized by different companies and researchers (e.g., Muliawan et al., 2013; Wan et al., 2016).

Wind and wave power are abundantly renewable in China. For offshore wind exploitation, the newly installed capacity of generation has reached 51,473 MW in the world; in particular, the top country is China, which contributes 45.1% to the total newly generation. The rapid investments of the new installed capacity of wind power are the

direct results of the Chinese government's policy (Liao, 2016). In addition, wave energy has also become a hot focus in some domestic research literature (Liang et al., 2013, 2014; Zheng et al., 2013; Wang et al., 2014, 2016).

In the north-western Pacific, the largest semi-enclosed marginal sea is the South China Sea (SCS). As is shown in Fig. 1, the SCS has a topographical advantage for renewable energy development. The SCS is connected to the surrounding seas, such as through the Strait of Malacca to the Indian Ocean, through the Gasper to the Sulu Sea, through the Karimata Straits to the Java Sea, through the Luzon Strait to the Pacific Ocean, and through the Taiwan Strait to the East China Sea. Wind and wave power potential is of great significance to oil and gas development, the fishing industry, Army garrisons, islander living, and tourism construction.

To our knowledge, a few existing investigations on surface winds and waves have been conducted in the SCS or other regions of the China Sea. Based on the long time series of daily averaged wind dataset, Jiang et al. (2013) estimated that the total 10 m wind power in China's offshore regions can up to be about 660 GW. Based on 23-year (1990–2012) historical wind fields, the offshore wind potential in Bohai was comprehensively analyzed and assessed (Wang et al., 2014). The

* Corresponding author. College of Engineering, Ocean University of China, Qingdao 266100. China.
E-mail address: dongsh@ouc.edu.cn (S. Dong).

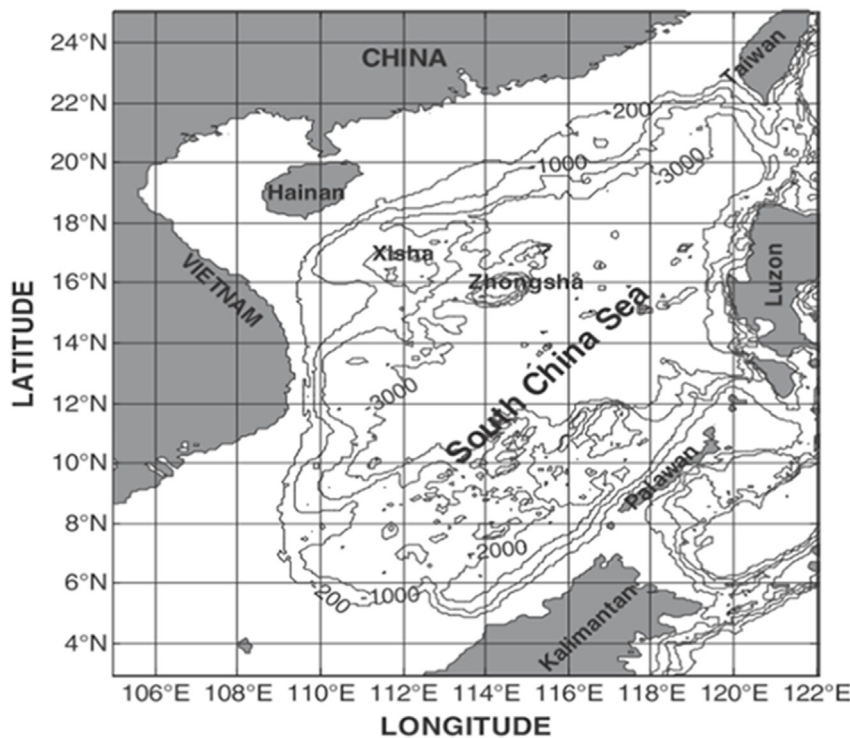


Fig. 1. The study domain in this paper: topography and depth of water in the South China Sea (m).

Table 1
Model set-up of the WRF.

Physical Process	Reference
Boundary	YSU (Hong et al., 2006)
Cloud	Kain-Fritsch (Kain and Fritsch, 1990)
Rad	Long: RRTMG (Mlawer et al., 1997) Short: RRTMG (Dudhia, 1989)
Land	Noah (Decharme, 2007)

assessment showed that the research domain had high-density wind power available. Chang et al. (2015) calculated the wind power density characteristics in the strait based on the double-parameter Weibull distribution function. The analysis indicates that the wind energy potential will be slightly larger in the eastern part of the Taiwan Strait in future climate periods, while they decrease by about 3% relative to the previous climate periods. Besides, there are relatively more wave climate and energy analyses than wind investigations in the SCS. The

Table 3
Comparisons of H_s between the simulation and observations when the typhoons passed through the region.

Typhoon	Observation time	Lon (E)	Lat (N)	Obs. (m)	Sim. (m)
Wayne	06:00 Sep 05, 1986	112°07.6'	19°32.8'	8.6	8.9
Brian	12:00 Sep 30, 1989	112°07.6'	19°32.8'	8.7	9.0

wave model was utilized to achieve the wave hindcast during the period when two cold fronts and two typhoons passed Hong Kong in the northern SCS (Wang et al., 1992). Kohei et al. (1998) analyzed the wave characteristics in a port near the Vietnam's central coastline in the SCS by utilizing real measurements from April 1997 to February 1998. Zhu et al. (2003) constructed a coupled numerical system of currents, tides, as well as waves in the coastal regions of the SCS under the extreme weather conditions such as the tropical cyclones. Similarly, Chu and Cheng (2008) analyzed the wave states when the typhoon Muifa crossed the SCS during the winter months in 2004. In addition, based on

Table 2
Validations of the reanalysis wind data at the three stations.

Month	Errors in wind speed (m/s)			Errors in wind direction (°)			Number of records		
	Dongsha	Xisha	Nansha	Dongsha	Xisha	Nansha	Dongsha	Xisha	Nansha
1	2.85	4.65	1.86	20.6	20.5	22.5	532	558	338
2	2.64	4.10	1.66	19.2	25.7	21.2	572	650	441
3	2.60	3.45	1.84	24.5	23.8	27.7	649	712	471
4	1.87	2.34	1.80	34.0	27.0	27.9	663	701	427
5	2.00	1.90	1.76	34.3	31.5	34.3	663	721	456
6	2.66	2.20	1.94	29.3	23.9	31.2	654	703	449
7	2.60	2.17	1.80	27.9	29.8	25.6	664	728	482
8	2.67	2.12	2.05	27.9	29.1	22.3	578	627	406
9	2.84	2.38	1.71	31.7	36.7	30.6	622	668	473
10	3.13	4.06	2.06	16.1	25.2	22.5	666	705	702
11	3.34	5.35	2.58	16.6	21.8	27.5	610	674	348
12	3.68	6.32	2.68	16.6	21.8	29.2	648	726	389
Average	2.73	3.40	1.96	25.1	26.4	29.6	7521	8173	5168

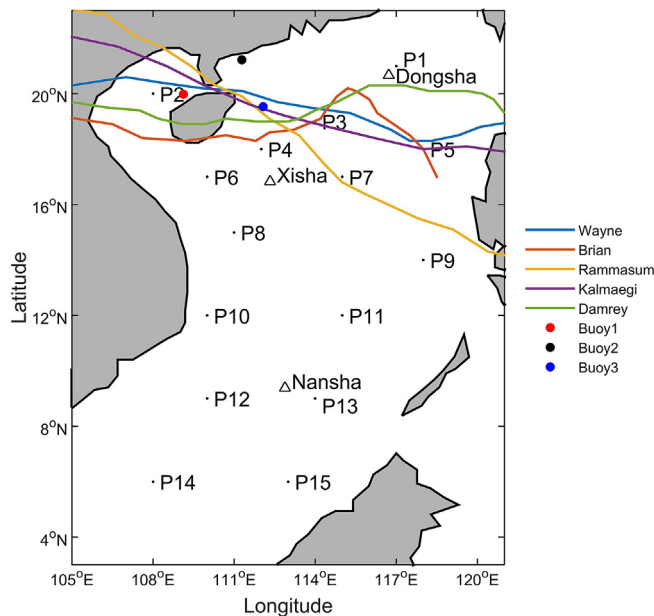


Fig. 2. Map of the wind and wave observation stations, typhoon tracks, and selected points for further wind and wave statistical analyses.

the hindcast data, the characteristics of wind-wave and the engineering environment in the SCS have been studied by Wang et al. (2014). Further, the influence of the wind-wave on the ocean circulation has been studied by Zhang et al. (2009). Regarding the power exploiting, Zheng et al. (2013) estimated the stored wave and wind power potential across the entire China Sea from 1988 to 2009 based on the CCMP wind dataset and wave hindcasts, but they provided a relatively inadequate analysis for the SCS. Mirzaei et al. (2015) simulated the waves and made an analysis of wave energy in the SCS forced but ignored wind energy.

The planning and operation of offshore wave energy converters and wind turbines is in need of dependable estimates of surface waves, wind field, and their long-term variabilities. However, it is rare to find a sufficient number of buoy observations with longer durations that can be selected to precisely determine the wind and wave fields over the entire domain. Although the aforementioned wind and wave studies have been conducted in the SCS, a systematic and reliable investigation on the long-run wind and wave conditions and variabilities are yet insufficient or lacking. Various researches have suggested that high-resolution model hindcasts for the wind and wave environment can offer appropriate alternatives for wind and wave fields statistics (Dallman et al., 2014). Hence, for this objective, this paper concentrates on providing a better understanding of the long-term temporal and spatial characteristics of wind and wave states in the SCS using model

hindcasts. The Weather Research and Forecasting model (WRF; Skamarock et al., 2008) is selected to obtain a 30-year wind hindcasts, and WAVEWATCH-III (WW III; Tolman, 2009) is continuously performed to simulate a 30-year wave hindcasts, driven by the wind-field hindcast derived from the WRF.

Therefore, we aim to accurately simulate the wind and wave fields from 1986 to 2015 using the high-resolution numerical models to fill the gap in the SCS wind and wave studies. We will accomplish this by determining the average available wave and wind energy potential and their seasonal and monthly variations. There are five sections in this paper. Methods of estimating the wave and wind power density in the SCS are outlined in section 2. The introduction of wind and wave numerical models, their detailed configurations, and the validated hindcast data are shown in section 3. Then the results and discussion are presented in section 4. Finally, the summary and conclusions are shown in section 5.

2. Methods for energy density estimation

2.1. Methods of wind energy estimation

The kinetic potential is defined as the energy that the air vertically crosses a section at a certain wind speed. It can be expressed as follows (Voivontas et al., 2001):

$$E_k = \frac{1}{2} m V^2 \quad (1)$$

where E_k , m , and V are the wind kinetic potential, the air mass, and the wind speed, respectively.

Besides, the air mass can be regarded as the product of between the air density and the air volume crossing the section during a certain period, hence, the E_k may be described as follows:

$$E_k = \frac{1}{2} (\rho A V t) V^2 = \frac{1}{2} \rho A V^3 t \quad (2)$$

where ρ , A and t are the air density, the sectional area, and the period, respectively.

Clearly, the wind energy potential is more affected by wind speed fluctuations due to the cubic relations and can be expressed as:

$$P(V) = \frac{1}{2} \rho A V^3 \quad (3)$$

Through the preceding mathematical derivation process, the wind energy density is greatly dependent on the wind speed and air density. Therefore it is finally summarized as follows:

$$P_d(\rho, V) = \frac{1}{2} \rho V^3 \quad (4)$$

where $P_d(\rho, V)$ is the basic unit to conduct the estimation of the energy stored in the wind. Herein, we take 1.292 kg/m^3 as the sea surface air density in the SCS.

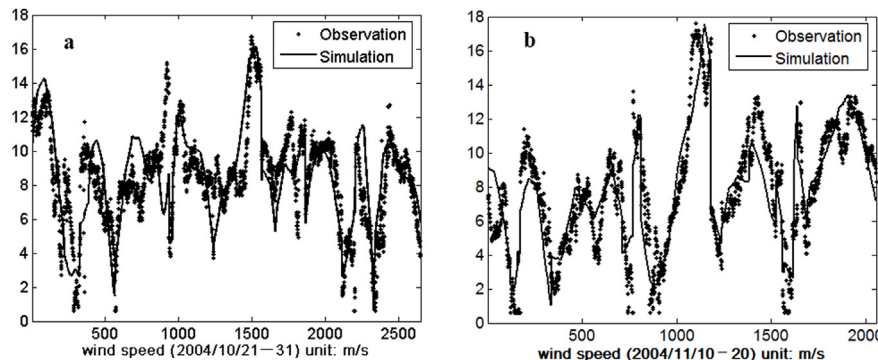


Fig. 3. Validations of the wind data between the simulations and the TOPEX/Poseidon altimeter data.

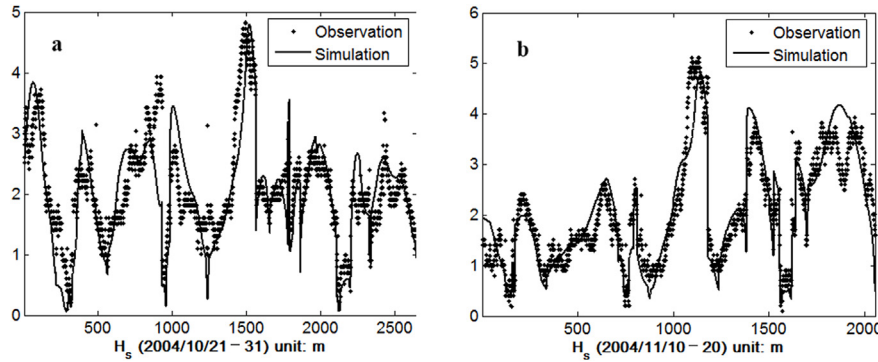


Fig. 4. Validations of H_s (m) between the simulation and the TOPEX/Poseidon altimeter data.

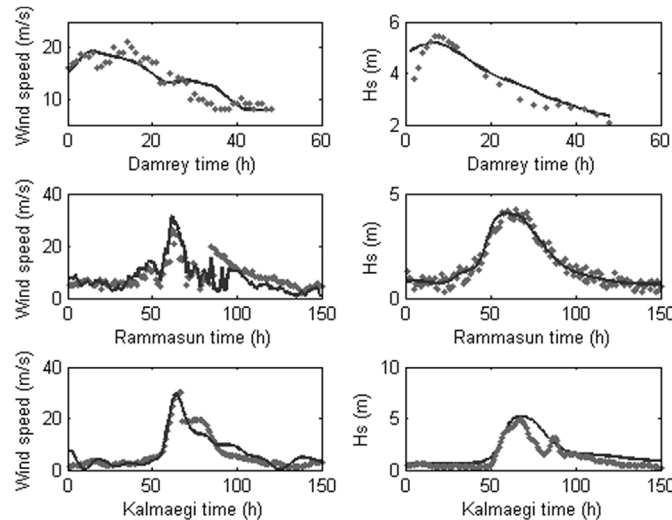


Fig. 5. Validations of the simulated and buoy-observed wind speeds and H_s as the typhoons progress.

2.2. Methods of wave energy estimation

Real waves can be universally regarded as the combination of various random wave conditions, including a great number of wave ingredients with different directions, amplitudes and frequencies. Further, the wave parameters can be described by the directional wave energy spectrum $E(\sigma, \theta)$. Therefore the wave power density, based on the wave spectrum, is

$$J = \rho g \int_0^{2\pi} \int_0^{\infty} C_g E(\sigma, \theta) d\sigma d\theta \quad (5)$$

where ρ , g , C_g , θ and σ are the seawater density, the gravity coefficient, the group velocity, the wave direction, and the relative frequency, respectively.

In deep-water regions, the wave power potential in per unit width of the progressing wave front, on the basis of the significant wave height and energy period, can as well as be described by (Tucker and Pitt, 2001)

$$J = \frac{\rho g^2}{64\pi} T_e H_s^2 \quad (6)$$

where T_e and H_s represent the significant period and the significant wave height, respectively.

Further, based on the following n th spectral moment, the spectral moments function can be utilized to determine the H_s and T_e :

$$m_n = \int_0^{2\pi} \int_0^{\infty} \omega^n E(\omega, \theta) d\omega d\theta \quad (7)$$

where $E(\omega, \theta)$ and ω represent the variance density spectrum and the absolute radian frequency in terms of the Doppler-shifted dispersion relation. Thus the T_e and H_s of wave conditions are described by respectively

$$H_s = 4\sqrt{m_0} \quad (8)$$

$$\text{and } T_e = \frac{m_{-1}}{m_0} \quad (9)$$

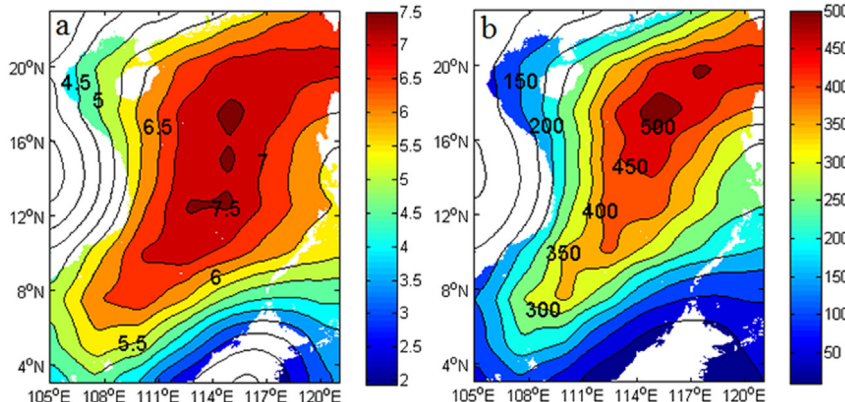


Fig. 6. The spatial patterns of (a) the annual wind speed (m/s) and (b) the wind energy potential (W/m^2).

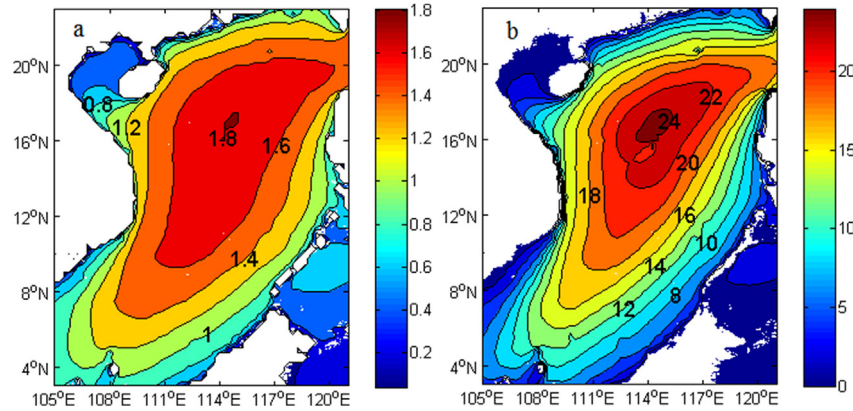


Fig. 7. The spatial patterns of (a) the annual significant wave height (m) and (b) the wave energy potential (kW/m).

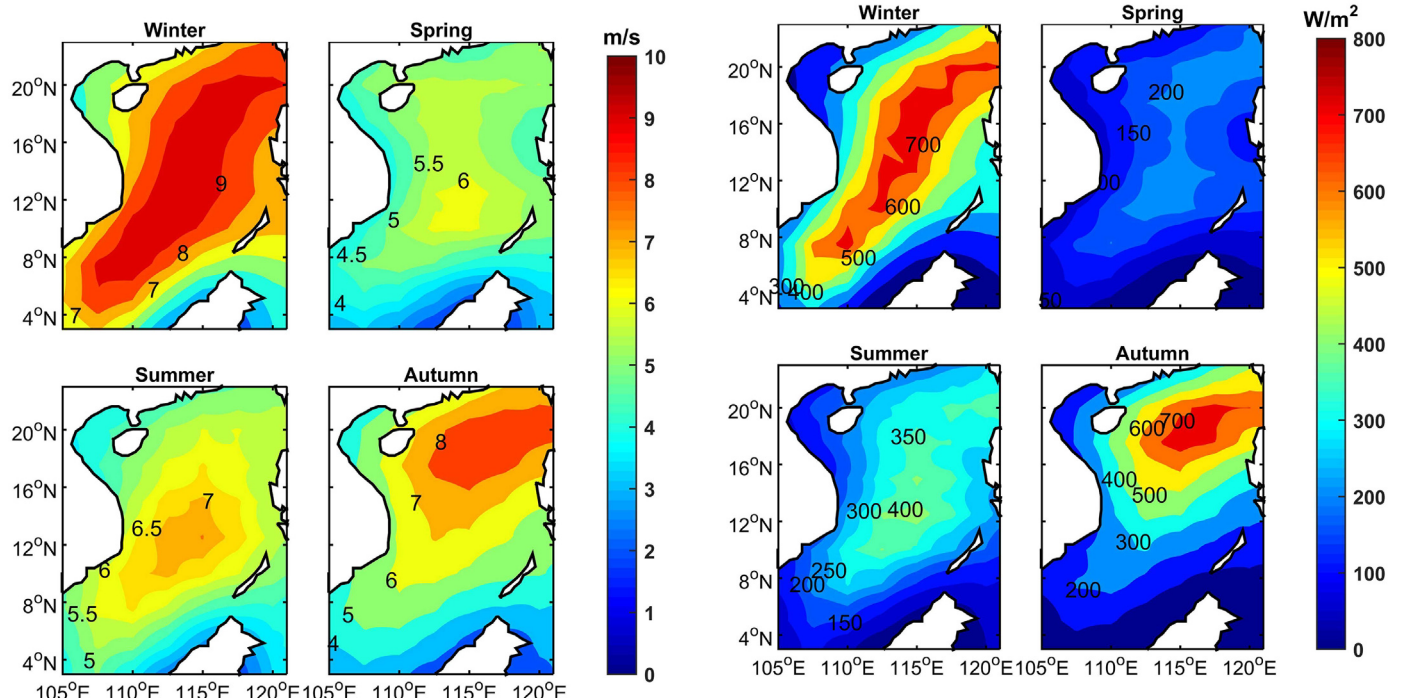


Fig. 8. The spatial patterns of the seasonal averaged wind speed (m/s).

3. Model description and hindcast configuration

3.1. Wind model description

The wind field is of great importance to perform the correct wind simulations, which are the basis of wave hindcasts. In this paper the WRF model, a mesoscale forecasting model as well as assimilation system, was selected to simulate the wind-field. The model contains physical processes and dynamic processes with climate change. Specifically, the ground-surface and cloud layers, the short-wave and long-wave radiation are considered into the atmospheric radiation scheme. The non-local K close or the second-order turbulence close scheme is used in the planetary boundary layer. Besides, as a non-static model, all the calculation processes such as atmospheric simulation, integrating numerical weather forecasting, and data assimilation are continuously processed based on the Arakawa C-grid.

Regarding the vertical direction in the WRF model, η can be written as follows:

$$\eta = (p_h - p_{ht})/\mu, \quad (10)$$

where p_{hs} and p_{ht} represent pressures, and $\mu = p_{hs} - p_{ht}$. Besides, the equations can be expressed as in Euler form:

$$\frac{\partial U}{\partial t} + (\nabla \cdot V u) - \mu_d \alpha \frac{\partial p}{\partial x} + (\alpha/\alpha_d) \frac{\partial}{\partial \eta} \left(\frac{\partial p}{\partial \eta} \frac{\partial \Phi}{\partial x} \right) = F_U \quad (11)$$

$$\frac{\partial V}{\partial t} + (\nabla \cdot V v) - \mu_d \alpha \frac{\partial p}{\partial y} + (\alpha/\alpha_d) \frac{\partial}{\partial \eta} \left(\frac{\partial p}{\partial \eta} \frac{\partial \Phi}{\partial y} \right) = F_V \quad (12)$$

$$\frac{\partial W}{\partial t} + (\nabla \cdot V w) - g \left[(\alpha/\alpha_d) \frac{\partial p}{\partial \eta} - \mu_d \right] = F_W \quad (13)$$

$$\frac{\partial \Theta}{\partial t} + (\nabla \cdot V \theta) = F_\theta \quad (14)$$

$$\frac{\partial \mu}{\partial t} + (\nabla \cdot V) = 0, \quad (15)$$

$$\frac{\partial \varphi}{\partial t} + \frac{1}{\mu} [(\nabla \cdot V \varphi) - gW] = 0 \quad (16)$$

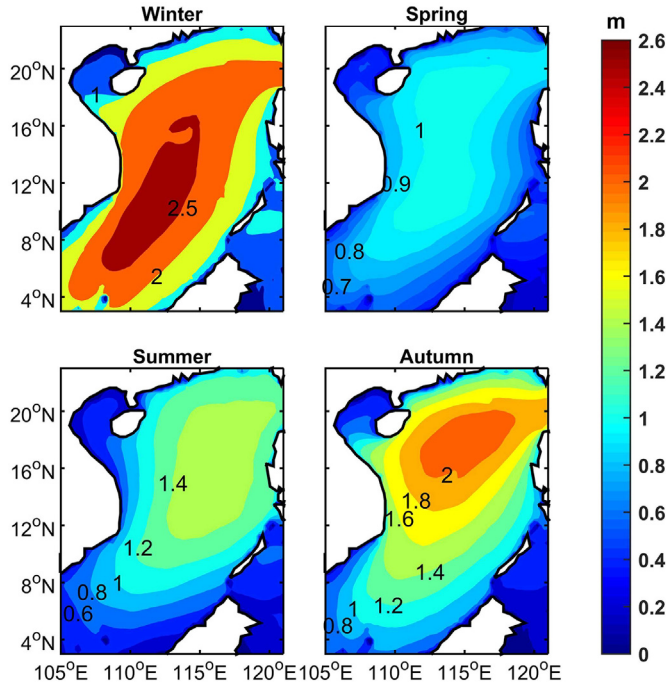


Fig. 10. The spatial patterns of the seasonal averaged wave significant heights (m).

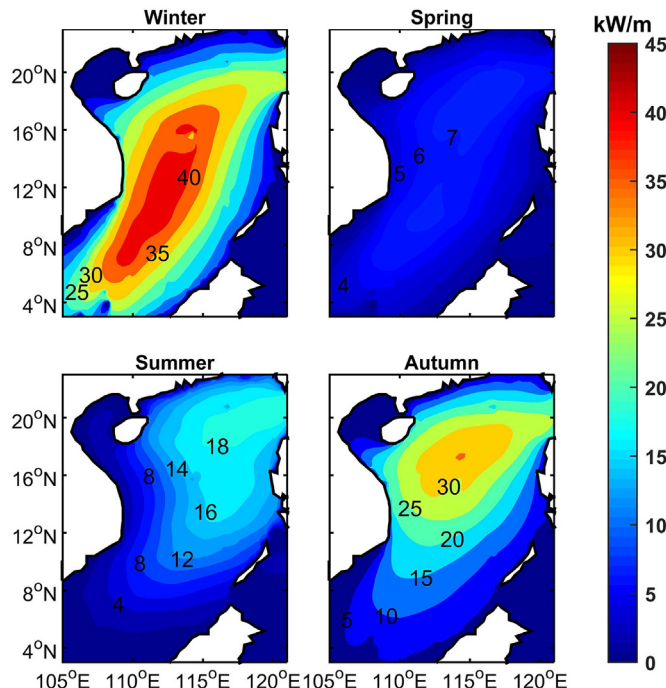


Fig. 11. The spatial patterns of the seasonal averaged wave energy potential (kW/m).

$$\text{and } \frac{\partial Q_m}{\partial t} + (\nabla \cdot V q_m) = F_{Qm} \quad (17)$$

where ϕ is potential, F is external force, μ is the friction coefficient, θ is potential temperature, q_m is the specific humidity, u , v and w represent the zonal, meridional and vertical wind components, g represents the gravity coefficient, and π represents the total Exner function.

3.2. Wind model set-up and validation

The WRF model is set at 0.2° by 0.2° in the horizontal resolution and simulated from January 1986 to December 2015 with hourly outputs. The simulated domain covers approximately between 20° longitude ($105^\circ\text{E} \sim 125^\circ\text{E}$) and 20° latitude ($3^\circ\text{N} \sim 23^\circ\text{N}$). Herein, 16 layers are set in the vertical direction, and the Yonsei University (YSU) scheme is selected for the lateral boundary. The National Centers for Environmental Prediction/National Center for Atmospheric Research (NCEP/NCAR) reanalysis is selected as the wind initial fields. The re-analysis is at 0.25° by 0.25° in the horizontal resolution and 3 h in temporal resolution.

The WRF model itself provides a very large number of physical options, such as an atmospheric boundary layer turbulence scheme, a cumulus parameterization scheme, a cloud microphysics scheme, short wave radiation, and sea- and land-surface processes. Based on our previous research experience and the characteristics of the SCS, the physical processes are chosen as shown in Table 1.

Comparative analysis is made between the observations and the hindcasts winds (Table 2). Three observation stations are chosen including Nansha station ($9^\circ23'\text{N}$, $112^\circ53'\text{E}$), Xisha station ($16^\circ50'\text{N}$, $112^\circ20'\text{E}$), and Dongsha station ($20^\circ40'\text{N}$, $116^\circ43'\text{E}$). The time span is 8768 h from 2000 to 2005. Results show that mean errors of the wind speeds and directions at Nansha Xisha, and Dongsha are 1.96 m/s and 29.6°, 3.4 m/s and 26.4°, and 2.73 m/s and 25.1°, respectively.

Further, comparisons are conducted between TOPEX/Poseidon altimeter observations and the hindcasts winds. Fig. 3 shows the two verifications of the wind speeds given by the altimetry observations and the assimilations. The tracks of TOPEX/Poseidon are from 21 to 31 October 2004 and 10–20 November 2004. Comparison results indicate that the assimilations wind fields are in consistent with the TOPEX/Poseidon data.

3.3. Wave model description

In this paper, the WW III, initially developed by NCEP, is chosen to perform the wave simulation. The model contains submodules such as the general governing transport equations that permit full coupling with ocean models, modified third-order propagation schemes, modified physics for wave growth and decay, and a modified physics integration scheme. Except that the NCEP utilizes the WW III to achieve regional and global wave forecasts, a great number of researchers have chosen it to investigate the dynamical behaviours of sea surface waves.

The wave model can better solve the spectral action density balance equation, and the non-linear energy interaction in terms of waves with different frequencies can be directly computed for the purpose of avoiding the shape limitation in the predictive spectra.

Regarding the wave propagation, it can be defined as by:

$$\frac{dN(k, \theta)}{dt} = \frac{S(k, \theta)}{\sigma}. \quad (18)$$

Herein, $N(k, \theta) = F(k, \theta)/\sigma$ represents the wave action density spectrum, of which $F(k, \theta)$ represents the wavenumber-directional spectrum, σ represents the intrinsic (radian) or relative frequency. Further, S represents the net effect of the source and sink for the spectrum $F(k, \theta)$, and θ and k represent the wave direction and wave number, respectively.

Besides, the equilibrium equation in terms of spectrum N can be written in Euler form:

$$\frac{\partial N}{\partial t} + \nabla_x \dot{x} N + \frac{\partial}{\partial k} \dot{k} N + \frac{\partial}{\partial \theta} \dot{\theta} N = \frac{S}{\sigma}, \quad (19)$$

$$\dot{x} = c_g + U, \quad (20)$$

$$\dot{k} = -\frac{\partial \sigma}{\partial d} \frac{\partial d}{\partial s} - k \frac{\partial U}{\partial s}, \quad (21)$$

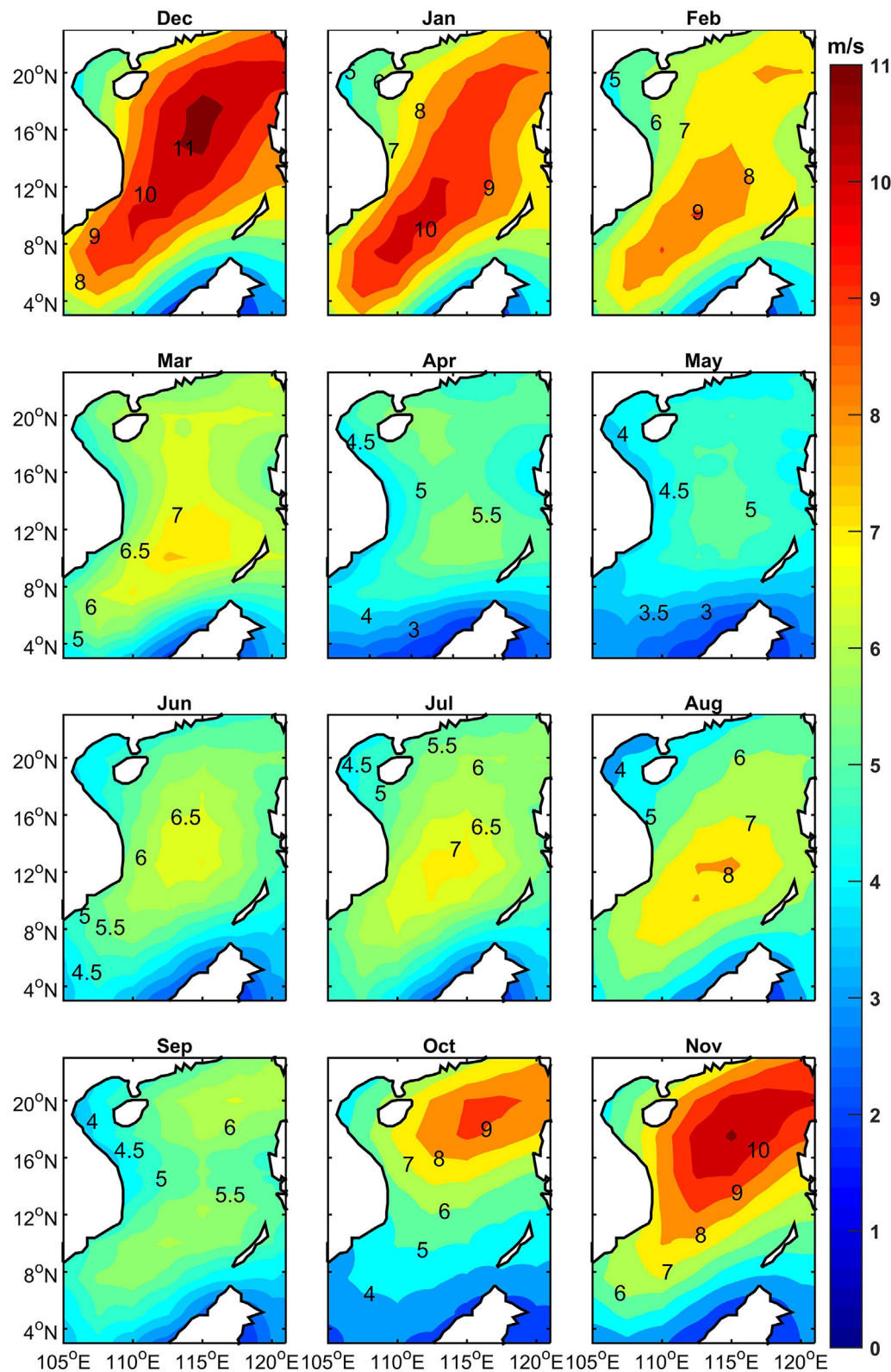


Fig. 12. The spatial patterns of the monthly averaged wind speed from December to November (m/s).

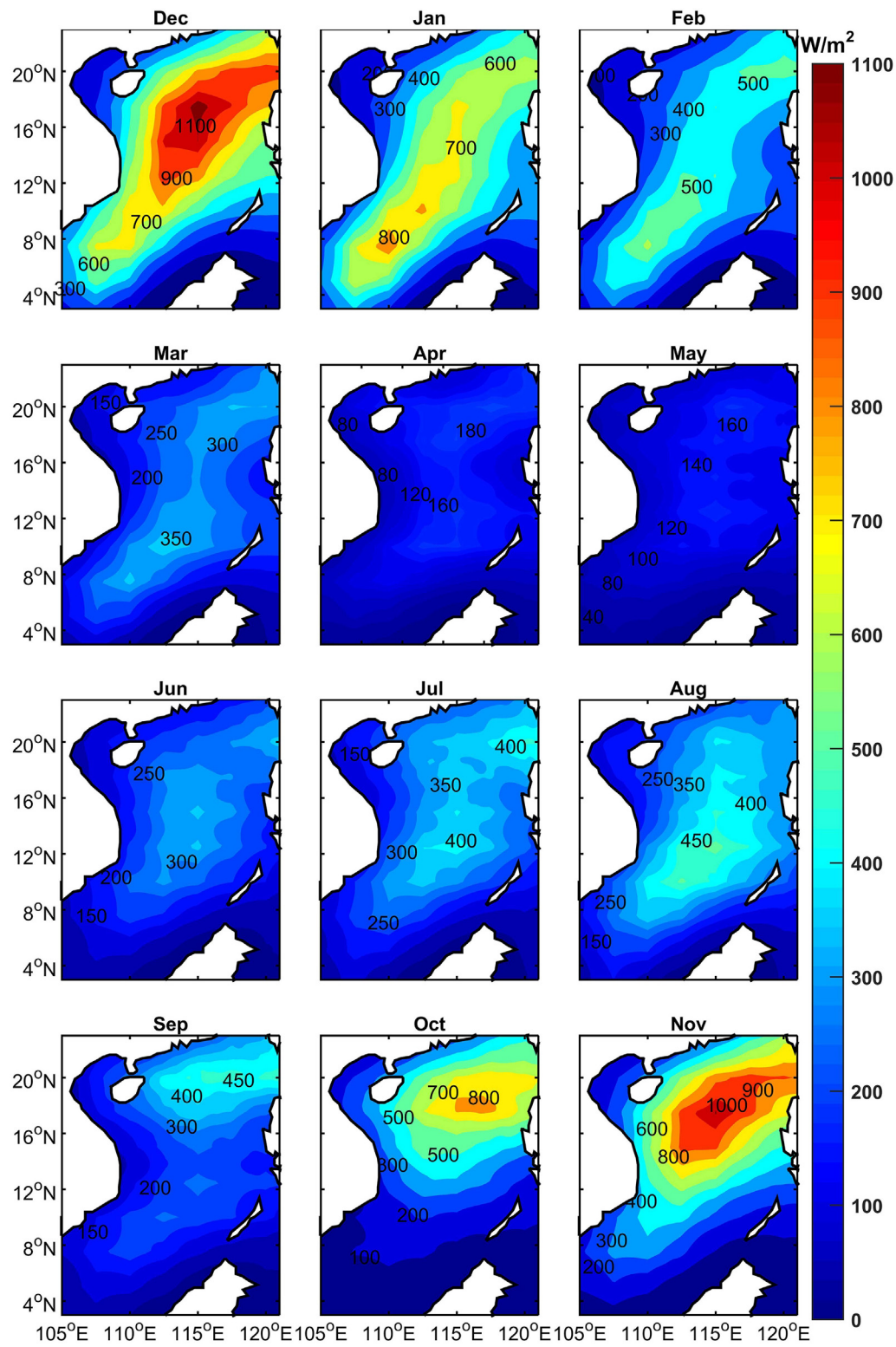


Fig. 13. The spatial patterns of the monthly averaged wind power density from December to November (W/m^2).

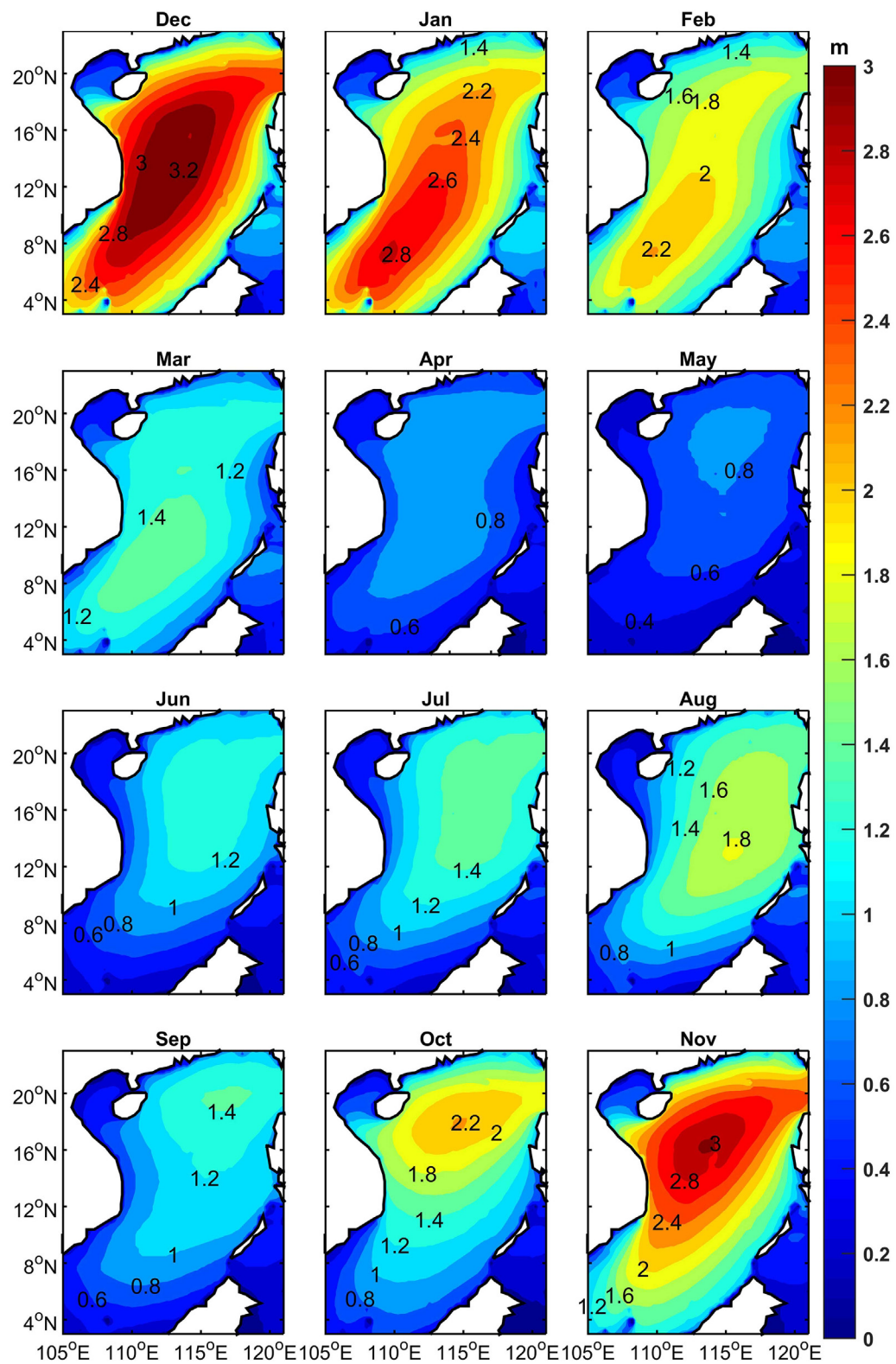


Fig. 14. The spatial patterns of the monthly averaged wave significant heights from December to November (m).

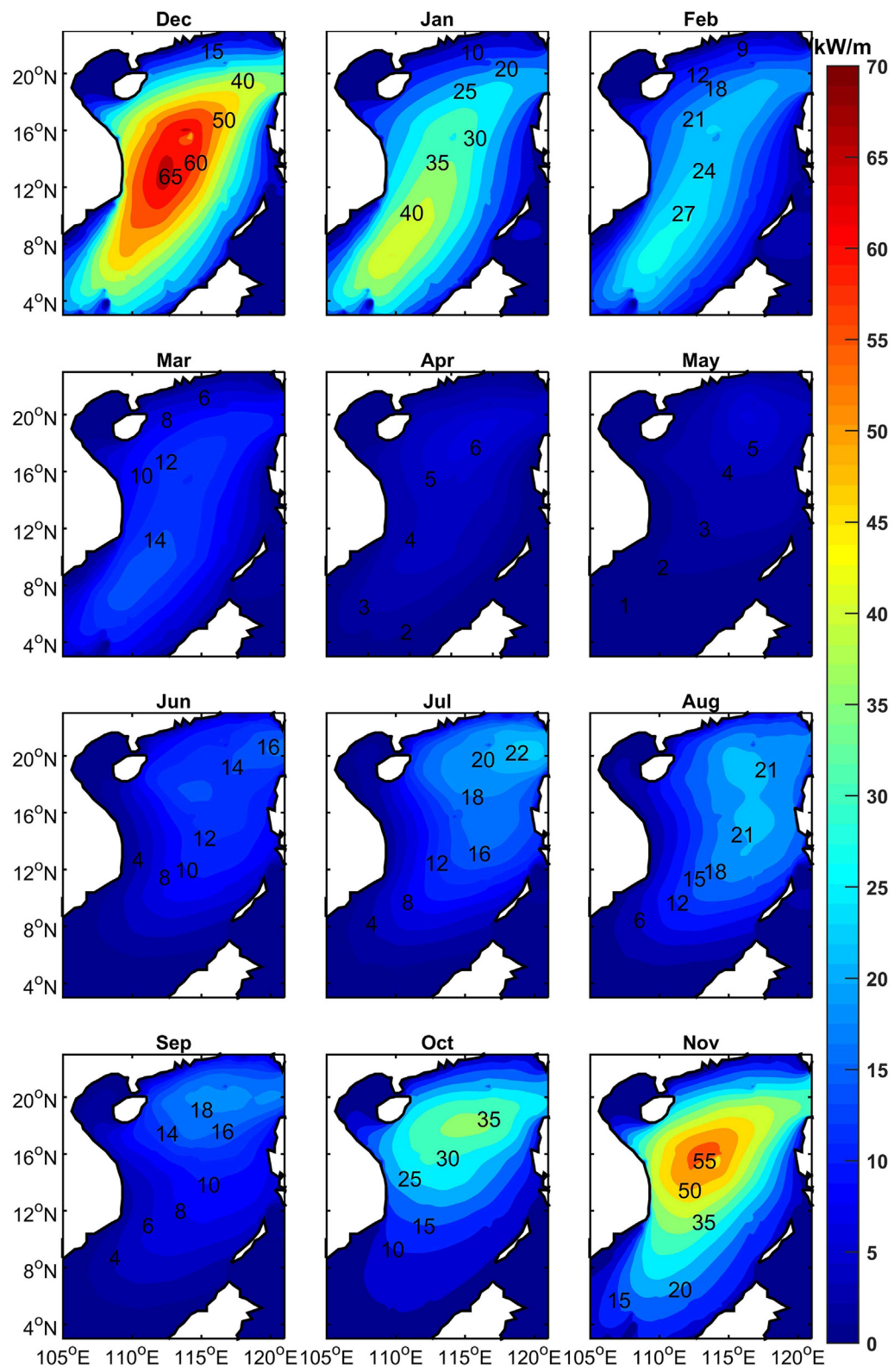


Fig. 15. The spatial patterns of the monthly averaged wave energy potential from December to May (kW/m).

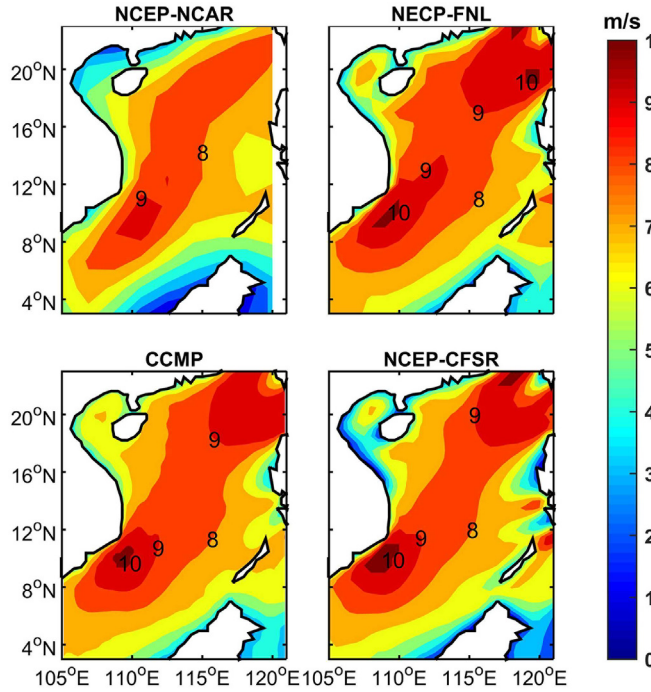


Fig. 16. Comparisons of mean wind speed among different wind datasets in January.

$$\text{and } \dot{\theta} = -\frac{1}{k} \left[\frac{\partial \sigma}{\partial d} \frac{\partial d}{\partial m} - k \frac{\partial U}{\partial m} \right], \quad (22)$$

where c_g can be determined by θ and c_g , s and m represent the coordinate in the direction and the coordinate perpendicular to s .

Regarding the net source term S , it is generally composed of three respects, including the wind–wave interaction term S_{in} , the non-linear wave–wave interaction term S_{nl} , and the dissipation (“white capping”) term S_{ds} . It must be noted that the S_{bot} cannot be neglected when in the shallow waters. Hence, the S can be defined as:

$$S = S_{in} + S_{nl} + S_{ds} + S_{bot}. \quad (23)$$

Specially, the input source term can be written as:

$$S_{in}(\sigma, \theta) = \sigma \beta N(\sigma, \theta), \quad (24)$$

where σ represents the non-dimensional wind–wave interaction parameter. Besides, the S_{nl} can be modelled based on the methods of discrete interaction approximations. The S_{ds} is determined by the linear combinations including the high-frequency component $S_{ds,h}$ and the low-frequency component $S_{ds,l}$:

$$S_{ds} = AS_{ds,1} + (1 - A)S_{ds,h}, \quad (25)$$

where A represents a parameter determined by the frequency approximation.

Regarding the bottom friction source term, it is described by:

$$S_{bot}(k, \theta) = 2\Gamma \frac{n - 0.5}{gd} N(k, \theta), \quad (26)$$

where Γ and n represent the empirical constant and the ratio of phase velocity to group velocity, respectively.

3.4. Wave model set-up and validation

The WW III model was basically implemented in a non-stationary mode on the basis of spherical coordinates. Specially, the model execution was set in 24 directions as well as 25 frequencies that are spaced logarithmically from 0.05 Hz using a frequency increment factor of 1.1 Hz. Herein, it is supposed that no currents are considered. The simulations were computed using a maximum global time-step of 900 s, a maximum Courant–Friedrichs–Lewy condition time-step for x - y of 950 s, a k -theta time-step of 900 s, and a minimum source term time-step of 300 s.

In the model setting, the wind input growths are considered in both linear and exponential expressions. In particular, the scheme for the wind input parameterization was presented by Chalikov and Belevich (1993) for the linear growth mode and by Komen et al. (1984) for the exponential growth mode. Further, in this model configuration, several parameters are also considered, such as the bottom friction, the white capping, and the dissipation induced by wave breaking due to shallow-sea effect.

The initial step in the wave computations is to determine the entire simulated region where the wave climate is aimed to be modelled. Thus a uniform, regular rectangular computing grid was used, which covers the entire SCS (Fig. 1). The grid resolution is set to 0.2° by 0.2°. The output time-step was selected to be 1 h. The wind input data are chosen and introduced at length in section 3.2. The simulated database span is set from 1 January 1986 to 31 December 2015.

The WW III output wave parameters in the dataset includes the mean wave direction; significant wave height H_s ; mean period T_{m01} ; the zero-up crossing period, equal to T_{m02} which is the mean period T_z based on in the narrow band approximation; the energy period T_e , represented by the spectral period T_{m-10} in terms of the spectral moments m_0 and m_{-1} ; the directional wave propagation; and the normalized spectral frequency width. Further, the wave energy potential is computed based on the space-time records of H_s and T_e obtained in this hindcast dataset.

Comparative analysis is made between the modelled hindcasts and the TOPEX/Poseidon data. Similarly with wind fields, validations of H_s are displayed in Fig. 4. Specially, the time spans consist of the same periods (in 21–31 October 2004 and in 10–20 November 2004) during which the TOPEX/Poseidon exactly passed over the SCS. The modelled hindcasts coincide well with the observations, indicating that the surface wave fields over the domain can be simulated well by the WW III model.

3.5. Hindcast validation under extreme typhoon conditions

Typhoons happen frequently during autumn and summer months over the domain and have important effects on the extreme H_s . In general, the measured wave records under typhoon conditions are especially scarce. However, in this study two-moment observations are measured during the passages of Typhoon Wayne (198616) and Typhoon Brian (198926). The comparisons and validations of H_s between the measured data obtained from Qinglan Station and modelled hindcasts when the typhoons exactly passed are shown in Table 3. Clearly, the hindcasts results are in good agreement with the measured records, which concludes that the WW III model is a reliable alternative method to reproduce the surface wave fields under typhoon processes over the SCS domain.

Furthermore, three additional typhoons—Damrey (200509), Rammassum (201409), and Kalmaegi (201415)—were used to validate the model. The typhoon tracks and buoy stations from which the observation data were obtained are showed in Fig. 2. Comparisons of the

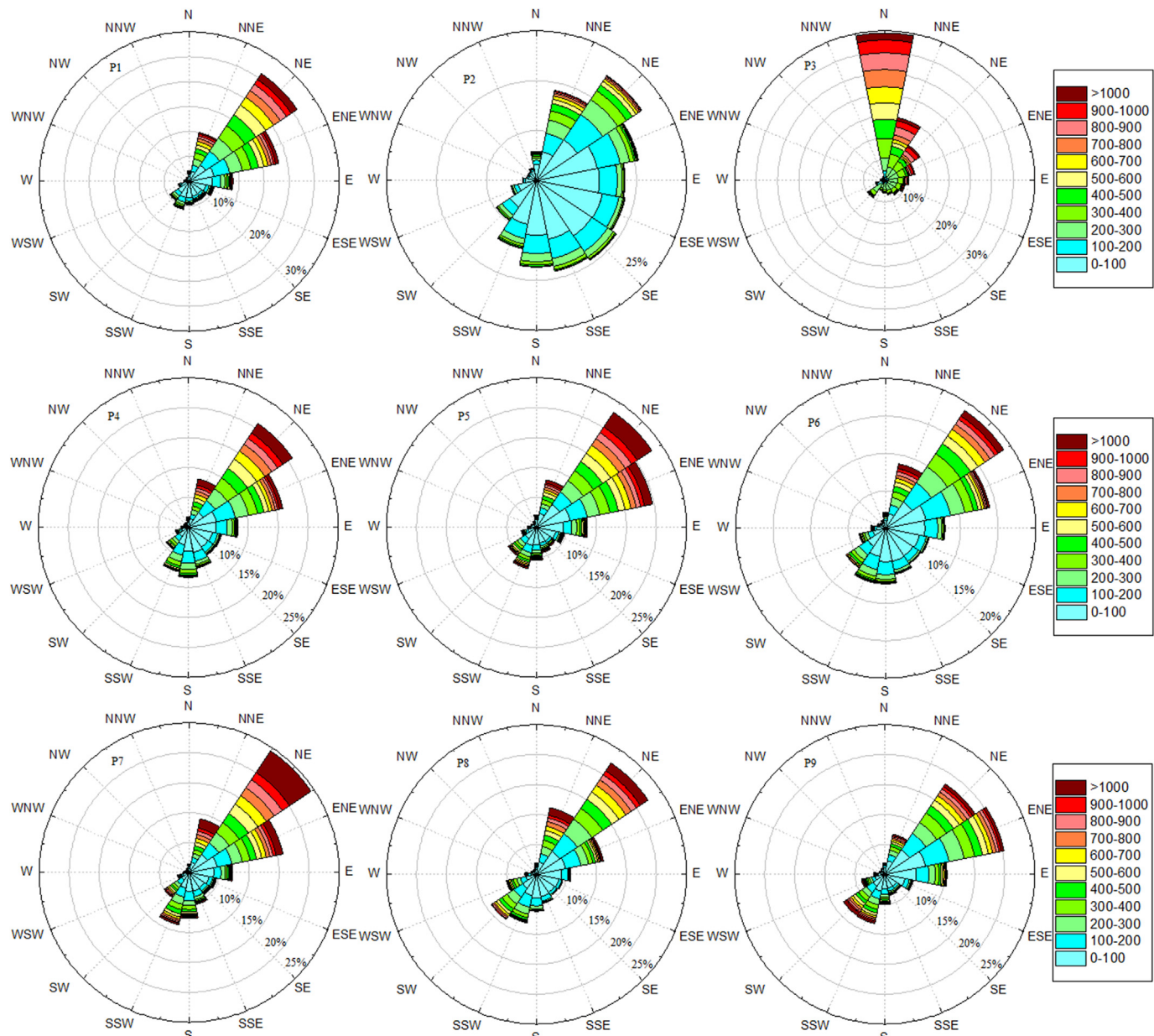


Fig. 17a. Wind power density roses at 15 chosen locations in the South China Sea.

simulated and observed wind speed and H_s are displayed in Fig. 5. The trend and values between the simulation and the observations show good consistency.

4. Results and discussion

4.1. Annual wind and wave energy estimation

In order to obtain the spatial patterns of wind and wave climate, a 30-year database simulated from the WRF and WW III models was chosen. Annual spatial patterns of wind and wave data were calculated from the total of 262,968 spatial records using the methods introduced

in section 2. Annual spatial patterns of wind speed and wind energy, significant wave heights, and wave power are obtained as contour maps in Figs. 6–7.

According to Fig. 6, wind speeds are between 4 and 7.5 m/s with 100–500 W/m² wind power density in most of the SCS. The largest wind speed, greater than 7.5 m/s, is in the middle of the SCS. The largest average wave energy is in the upper-middle in the SCS, with a value greater than 500 W/m². The wind power density is relatively low along the coasts, potentially because it is dissipated due to land effects. Herein, offshore represents the areas with deeper depths and greater distances from the coastlines.

Similar distributions for significant wave heights as well as wave

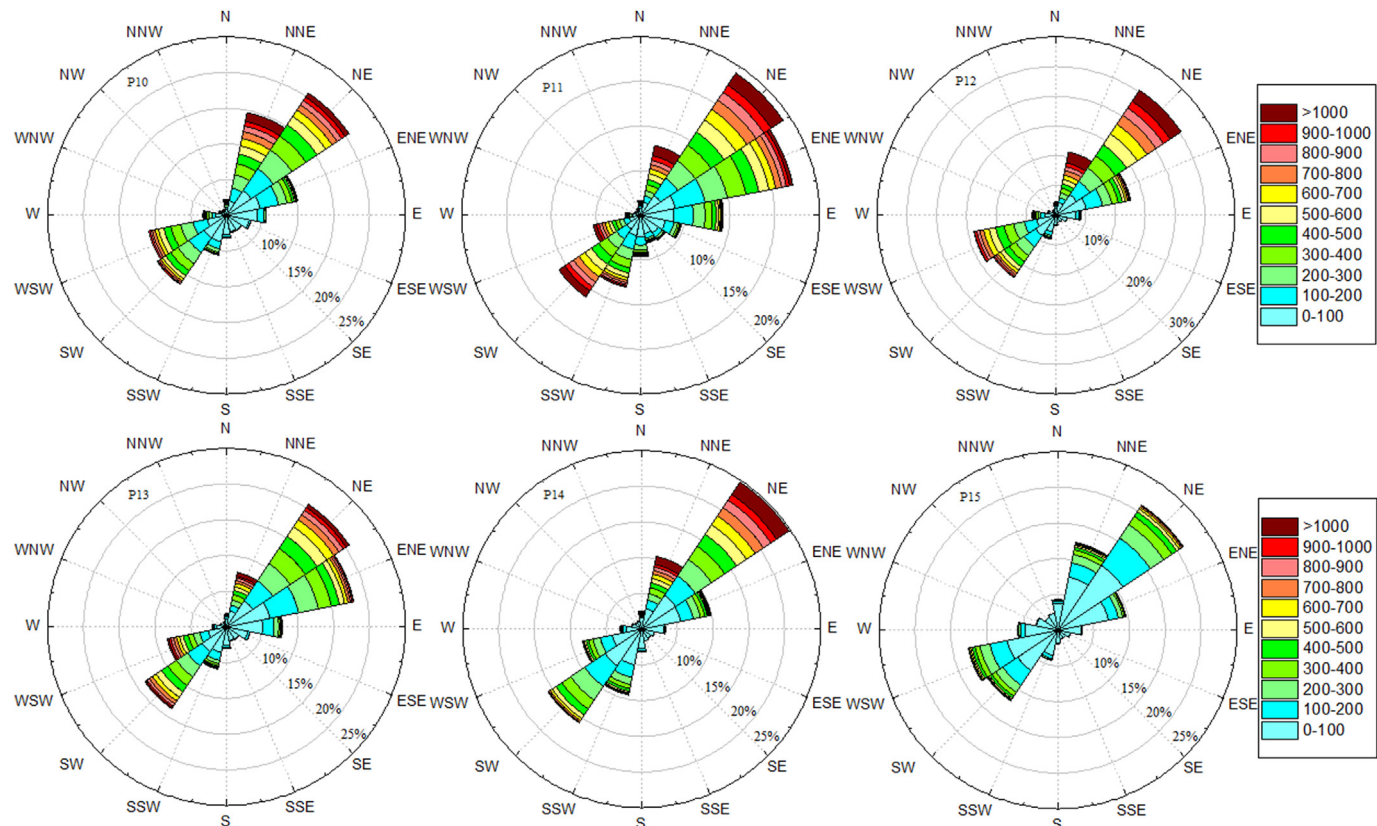


Fig. 17b. Wind power density roses at 15 chosen locations in the South China Sea.

energy are also obtained in Fig. 7. The wave power is relatively stronger offshore than nearshore, which is likely as a result of that the wave potential becomes dissipating induced by depth-water effects. Most waves are of H_s between 0 and 1.8 m with 0–24 kW/m potential density in the domain. The largest H_s exceeding 1.8 m occurs in the middle of the SCS. The largest mean energy density is around the same location greater than 24 kW/m. Therefore, both the wave power and wind power have the same geographical distribution characteristics. Results of simulated annual averaged wave energy in the present study are relatively larger than those simulated by Lin et al. (2017). This is perhaps due to different wind input data. Lin et al. (2017) used the Cross-Calibrated Multi-Platform (CCMP) wind field to simulate the waves in the SCS; however, the CCMP wind is relatively lower than the simulated wind in this paper.

4.2. Seasonal wind and wave energy estimation

Furthermore, the analysis of seasonal spatial patterns of wind speed and wind energy, significant wave heights, and wave power are also important to promote the understanding of wind and wave behaviours. Such spatial patterns are shown in contour maps Figs. 8–11.

Fig. 8 presents the mean seasonal spatial patterns of wind fields. The mean wind speed is lowest during spring, and becomes increases in the summer, autumn, and becomes strongest in winter. In winter, the wind with speeds between 7 and 10 m/s occurs in most of the SCS while in spring the speeds are primarily less than 6 m/s. In autumn, the larger wind speeds more than 8 m/s appears in the north-eastern area. In other

seasons the larger speeds appears in the central area. Fig. 9 shows the mean seasonal spatial patterns of wind energy density. The distributions are identical to the wind fields. The largest wind power density ($> 700 \text{ W/m}^2$) occurs in winter, while the lowest, once again, occurs in spring. Furthermore, the locations of larger wind energy flux are similar with the larger wind speeds accordingly.

Figs. 10 and 11 show the mean monthly spatial patterns of significant wave heights and energy potential. Similarly, the highest significant wave heights and potential fluxes ($> 2.5 \text{ m}$ and $> 40 \text{ kW/m}$, respectively) occur in winter while they decline to their minima in spring. Spatially, in winter both the significant wave height and the potential density are of their maxima in south-western parts of the SCS; in spring, they are at their maxima in the central SCS; from summer to autumn, they are at their maxima in northeastern parts of the SCS. Therefore, we can conclude that both the wind and wave have an obvious seasonal variation. The seasonal wave energy results in the present study are in good agreement with those by Mirzaei et al. (2015) and are relatively larger than those by Lin et al. (2017).

4.3. Monthly wind and wave energy estimation

Wind and wave characteristics, and their stored energy density, are relied on weather states. Thus, they might vary from daily and monthly. Mean monthly spatial patterns of wind speed and energy density, significant wave height, and wave energy density are thus calculated based on the average of the hindcasts data in the same month across the 30-year study period.

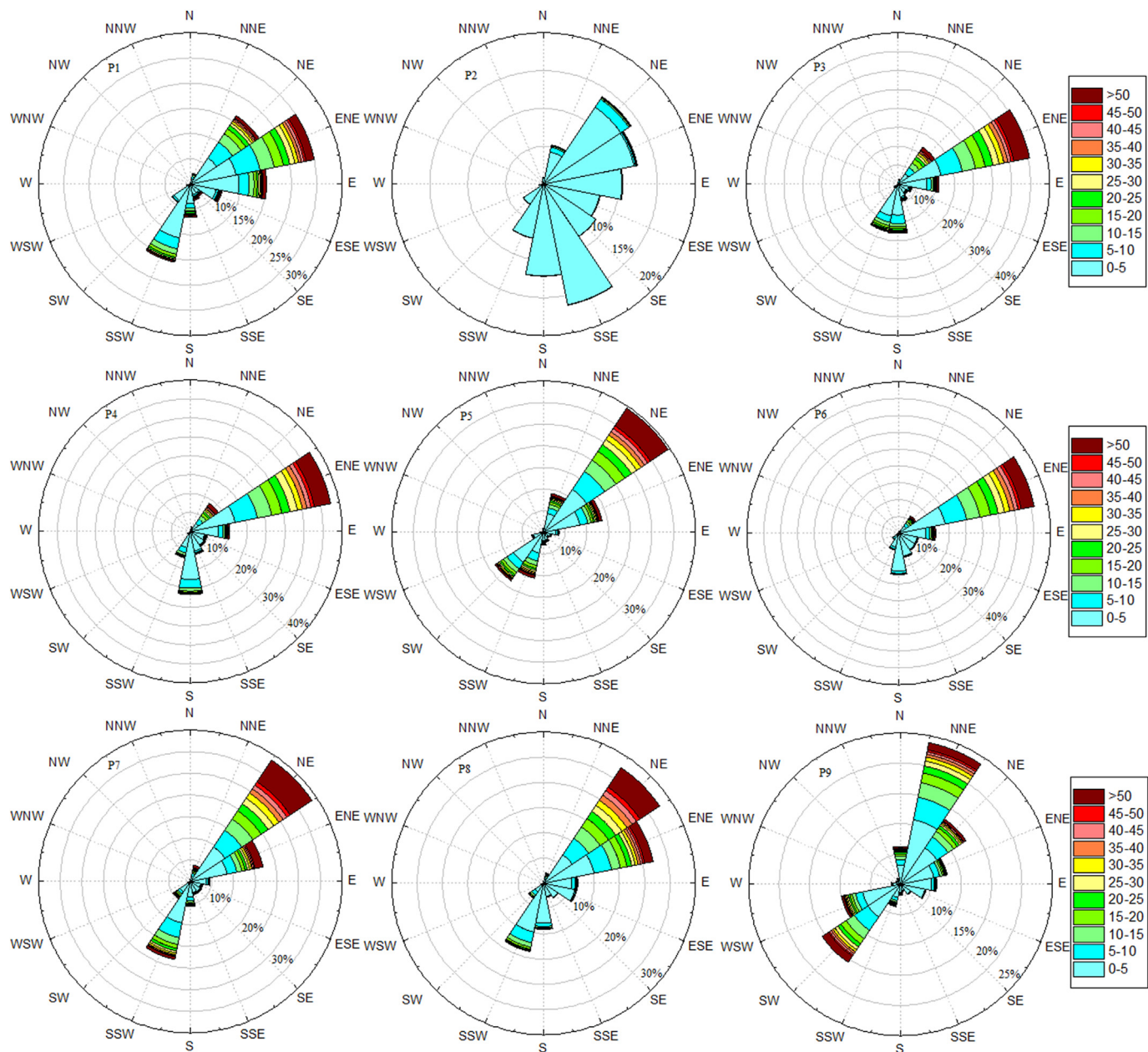


Fig. 18a. Wave energy roses at 15 chosen locations in the South China Sea.

Fig. 12 presents the mean monthly spatial patterns of wind fields. The largest wind speed ($> 11 \text{ m/s}$) occurs in December, while the minimum wind speed occurs in May. **Fig. 13** shows the mean monthly spatial patterns of wind energy density. The distributions are identical to the wind fields. The largest wind power density ($> 1100 \text{ W/m}^2$) occurs in December, while the lowest, once again, occurs in May. Furthermore, from January to March, both the wind speed and power potential are at their maxima in the south-western portion of the SCS; from April to August, they are at their maxima in the central SCS; and, from September to December, they are at their maxima in the north-eastern parts of the SCS.

Fig. 14 and **Fig. 15** show the mean monthly spatial patterns of

significant wave heights and energy potential. Similarly, the highest significant wave heights and potential fluxes ($> 2.8 \text{ m}$ and $> 65 \text{ kW/m}$, respectively) occur in December, while they decline to their minima in May. Spatially, from January to March, both the significant wave height and the potential density are of their maxima in south-western parts of the SCS; from April to August, they are at their maxima in the central SCS; and, from September to December, they are at their maxima in north-eastern parts of the SCS. Therefore, we can conclude that the wave characteristics are probably reliable indicators of the wind conditions, as they both exhibit similar variations in features.

In this study, the monthly results in January present a difference with Lin et al. (2017) and Arinaga and Cheung (2012). In the northeast

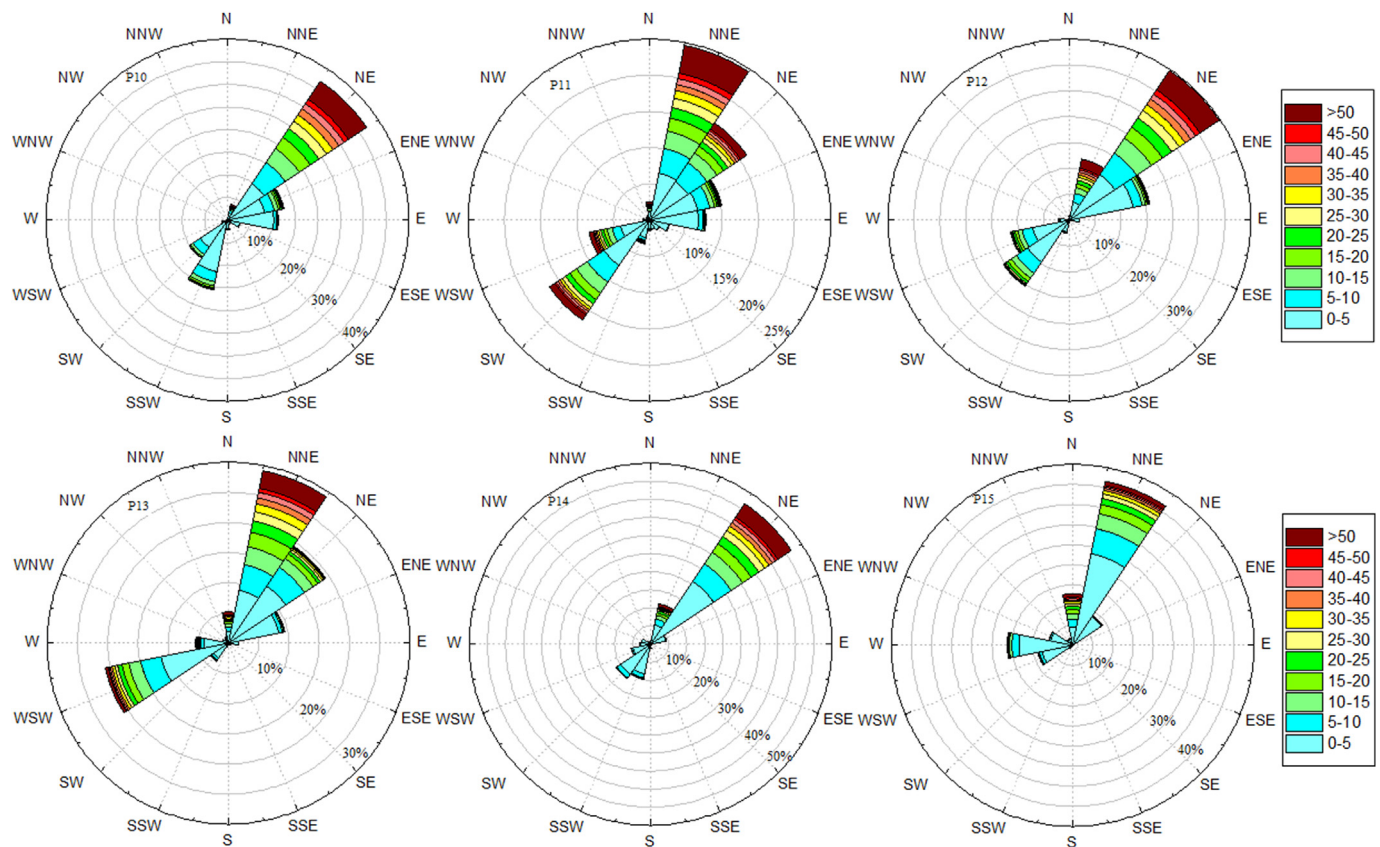


Fig. 18b. Wave energy roses at 15 chosen locations in the South China Sea.

of SCS, Lin et al. (2017) and Arinaga and Cheung (2012) showed a high-energy zone. The difference is due to different wind input data. Lin et al. (2017) used the CCMP wind fields and Arinaga and Cheung (2012) used the NCEP Final Global Tropospheric Analysis (FNL) wind data. The NCEP/NCAR reanalysis is selected as the wind initial fields in this paper. We have calculated the monthly wind fields in January for four different wind data with results shown in Fig. 16. The four different wind data show a difference in the northeast but the overall distributions in the all wind data are consistent. Moreover, the uncertain reasons of this difference need further research in the future because of the limit of measure data.

4.4. Statistical analysis of the wind and wave parameters

In order to study the directional characteristics of the wind and wave energy density in different regions, Fig. 17a and b presents the wind and wave energy potential, respectively, on the basis of the 30-year simulated hindcasts at 15 points (see Fig. 2). The directions of the NNE, NE, and ENE waves play important roles in most of the SCS. NE waves are the dominant direction at most points, while the dominant direction of region P3 is N and the dominant direction of P9 is ENE. Directions from the NNE to the SW are the most common wind directions in the Beibu Bay (region P2), which is influenced by monsoons and surrounding land masses.

Fig. 18a and b presents the wave direction distributions. Much like in the case of wind distributions, the directions of the NNE, NE, and ENE waves play important roles in most of the SCS. In the north-

western portion of the SCS, ENE waves are the most dominant type (i.e., in regions P1, P3, P4, and P6), while the dominant direction is NNE in the eastern SCS (i.e., in regions P9, P11, P13, and P15). In the open sea of the SCS (i.e., in regions P5, P7, P8, P10, P12, and P14), NE waves contribute most of the wave power flux. NE and SSE are also the recurring wave directions in the Beibu Bay (region P2). Therefore, wind-wave is the dominant wave pattern in the SCS.

To better make clear the constitutions of the wave power resources in terms of the wave periods and heights, the simulated records at 15 points are shown using a pattern of joint energy and scatter graphics in Fig. 19a and b. These graphics represent the occurrence of diversified wave conditions, on the basis of the wave energy periods, significant wave heights, and their own contribution to the annual mean energy based on the 30-year simulated wave database. The analysis is required to make sure the better performance of the diversified wave power converters at fixed positions in terms of the methods presented by Dunnett and Wallace (2009).

The sub-region within the joint energy and scatter graphics is classified into the standard squares with 1 m and 1 s. The numbers in every square represent the occurrences (the number of hours) of wave conditions with energy periods and significant wave heights belong exactly to the homologous classification. The lower numbers in the upper regions of the graphics indicate the low possibility of enormously larger waves.

This indicates that the range of energy periods is broad in the SCS, and the majority of wave energy is offered by wave energy periods with 2–15 s and significant wave heights with 0–12 m. Higher-value wave

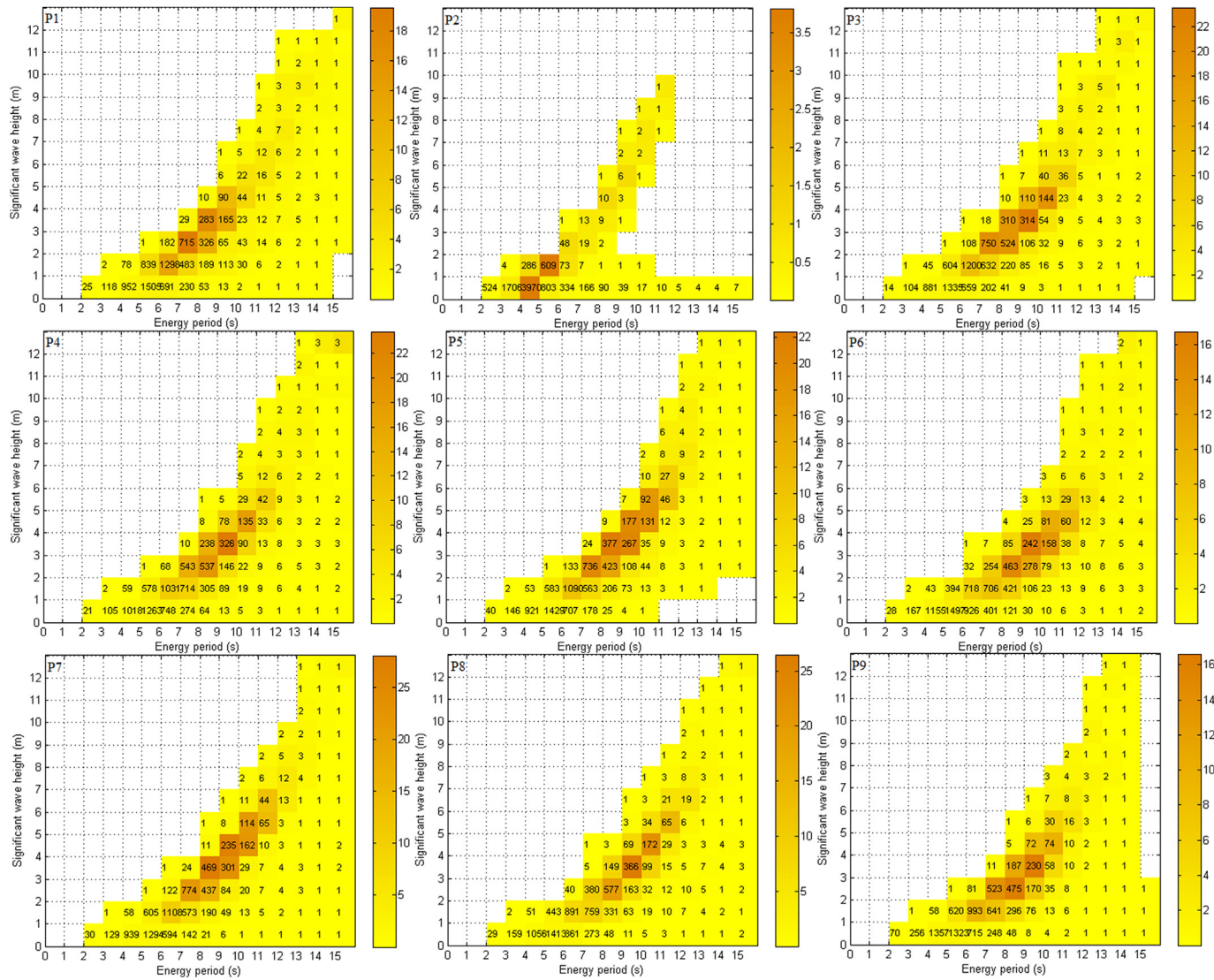


Fig. 19a. Combined energy and scatter graphics of the annual energy in terms of wave conditions at 15 chosen locations of T_e and H_s (the colour scale indicates the total annual power per meter in wave front, and the numbers represent the occurrences of wave conditions using number of hours per year). (For interpretation of the references to colour in this figure legend, the reader is referred to the Web version of this article.)

power, however, are supplied by energy periods with 6–11 s and significant wave heights with 1–6 m.

5. Conclusions

This paper put forward a further investigation on the wind and wave power resources in the SCS. Wind and wave states were continuously simulated based on the WRF and WW III model from 1986 to 2015 in the SCS.

Comparisons of the simulated and observed wind and wave fields show good agreement, even under extreme typhoon occurrences. Results show that the wind and wave energy have similar spatial and

temporal distributions. The winds and waves offshore, whose annual energy densities are up to be 1100 W/m^2 and 65 kW/m , respectively, are higher than they are inland or nearshore in general. The mean wind and wave potential are smallest in the spring and reach increasingly larger values during summer, autumn, and winter, in turn. The prevailing wind directions are NNE, NE, and ENE in most of the SCS regions. Higher values of wave power are offered by energy periods with 6–11 s and significant wave heights with 1–6 m.

In a summary, this investigation promotes the analysis of wind and wave behaviours in the SCS and generates a reliable database for further wind and wave environmental research and resource assessments.

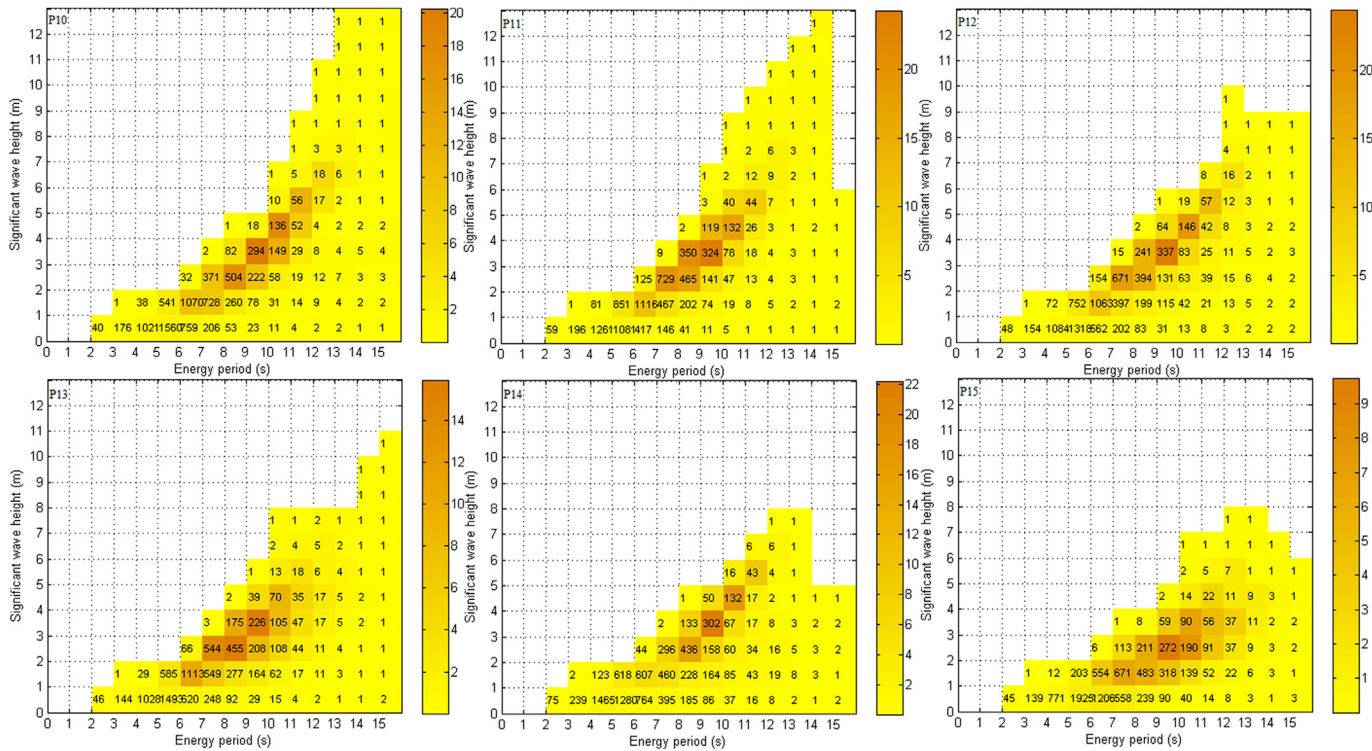


Fig. 19b. Combined energy and scatter graphics of the annual energy in terms of wave conditions at 15 chosen locations of T_c and H_s (he colour scale indicates the total annual power per meter in wave front, and the numbers represent the occurrences of wave conditions using number of hours per year). (For interpretation of the references to colour in this figure legend, the reader is referred to the Web version of this article.)

Acknowledgements

This work is financially supported by the National Natural Science Foundation of China (nos. 51509226 and 51479183).

References

- Akpınar, A., Bingölbaşı, B., Vledder, G.P.V., 2016. Wind and wave characteristics in the black sea based on the swan wave model forced with the cfsr winds. *Ocean Eng.* 126, 276–298.
- Arinaga, R.A., Cheung, K.F., 2012. Atlas of global wave energy from 10 years of reanalysis and hindcast data. *Renew. Energy* 39 (1), 49–64.
- Chalikov, D.V., Belevich, M.Y., 1993. One-dimensional theory of the wave boundary layer. *Boundary-Layer Meteorol.* 63 (1), 65–96.
- Chang, T.J., Chen, C.L., Tu, Y.L., Yeh, H.T., Wu, Y.T., 2015. Evaluation of the climate change impact on wind resources in Taiwan Strait. *Energy Convers. Manag.* 95, 435–445.
- Chu, P.C., Cheng, K.F., 2008. South China Sea wave characteristics during typhoon Muifa passage in winter 2004. *J. Oceanogr.* 64 (1), 1–21.
- Dallman, A.R., Neary, V.S., Stephenson, M., 2014. Investigation of Spatial Variation of Sea Offshore of Humboldt Bay, CA Using a Hindcast Model. Sandia National Laboratories, Sandia rep., Sand, pp. 2014–18207.
- Decharme, B., 2007. Influence of runoff parameterization on continental hydrology: comparison between the noah and the isba land surface models. *J. Geophys. Res. Atmos.* 112 (D19), D19108.
- Dudhia, J., 1989. Numerical study of convection observed during the winter monsoon experiment using a mesoscale two-dimensional model. *J. Atmos. Sci.* 46 (46), 3077–3107.
- Dunnett, D., Wallace, J.S., 2009. Electricity generation from wave power in Canada. *Renew. Energy* 34 (1), 179–195.
- Hong, S.Y., Noh, Y., Dudhia, J., 2006. A new vertical diffusion package with an explicit treatment of entrainment processes. *Mon. Weather Rev.* 134 (9), 2318–2341.
- Jiang, D., Zhuang, D., Huang, Y., Wang, J., Fu, J., 2013. Evaluating the spatio-temporal variation of China's offshore wind resources based on remotely sensed wind field data. *Renew. Sustain. Energy Rev.* 24, 142–148.
- Kamranzad, B., Etemad-Shahidi, A., Chegini, V., 2013. Assessment of wave energy variation in the Persian gulf. *Ocean Eng.* 70 (6), 72–80.
- Kain, J.S., Fritsch, J.M., 1990. A one-dimensional entraining/detraining plume model and its application in convective parameterization. *J. Atmos. Sci.* 47 (23), 2784–2802.
- Kohei, N., Shinji, K., Dao, Q.X., 1998. Wave characteristics on the central coast of Vietnam in the south China sea. *Coast Eng. J.* 40 (4), 347–366.
- Komen, G.J., Hasselmann, K., Hasselmann, K., 1984. On the existence of a fully developed wind-sea spectrum. *J. Phys. Oceanogr.* 14 (8), 1271–1285.
- Liang, B., Fan, F., Yin, Z., Shi, H., Lee, D., 2013. Numerical modelling of the nearshore wave energy resources of Shandong peninsula, China. *Energy Rev.* 57, 330–338.
- Liang, B., Fan, F., Liu, F., Gao, S., Zuo, H., 2014. 22-year wave energy hindcast for the China east adjacent seas. *Renew. Energy* 71 (11), 200–207.
- Liao, Z., 2016. The evolution of wind energy policies in China (1995–2014): an analysis based on policy instruments. *Renew. Sustain. Energy Rev.* 56, 464–472.
- Lin, G., Shao, L.T., Zheng, C.W., Chen, X.B., Zeng, L.F., Liu, Z.H., Li, R.B., Shi, W.L., 2017. Assessment of wave energy in the south China sea based on GIS technology. *Adv. Meteorol.* 2017. <http://dx.doi.org/10.1155/2017/1372578>.
- Mirzaei, A., Tangang, F., Juneng, L., 2015. Wave energy potential assessment in the central and southern regions of the South China Sea. *Renew. Energy* 80, 454–470.
- Mlawer, E.J., Taubman, S.J., Brown, P.D., Iacono, M.J., Clough, S.A., 1997. Radiative transfer for inhomogeneous atmospheres: RRTM, a validated correlated-k model for the longwave. *J. Geophys. Res. Atmos.* 102 (D14), 16663–16682.
- Muliawan, M.J., Karimrad, M., Gao, Z., Moan, T., 2013. Extreme responses of a combined spar-type floating wind turbine and floating wave energy converter (stc) system with survival modes. *Ocean Eng.* 65 (2), 71–82.
- Skamarock, W., Klemp, J., Dudhia, J., Gill, D., Barker, M., Duda, K., Huang, X.Y., Wang, W., Powers, J.G., 2008. A Description of the Advanced Research WRF Version3. pp. 1–113 report No. NCAR/TN-475+STR. Boulder, Colorado, USA.
- Tolman, H.L., 2009. User Manual and System Documentation of WAVEWATCH-iii Version 3.14. pp. 1–194 NOAA/NWS/NCEP/MMAB Technical Note, Washington.
- Tucker, M.J., Pitt, E.G., 2001. Waves in Ocean Engineering. Elsevier, New York.
- Ueckerdt, F., Brecha, R., Luderer, G., 2015. Analyzing major challenges of wind and solar variability in power systems. *Renew. Energy* 81, 1–10.
- Voivontas, D., Misirlis, K., Manoli, E., Arampatzis, G., Assimakopoulos, D., Zervos, A., 2001. A tool for the design of desalination plants powered by renewable energies. *Desalination* 133, 175–198.
- Wan, L., Gao, Z., Moan, T., Lugni, C., 2016. Comparative experimental study of the

- survivability of a combined wind and wave energy converter in two testing facilities. *Ocean Eng.* 111, 82–94.
- Wang, W.Z., Chen, J.C., Li, M.Q., 1992. Wind waves simulation in the north area of the south China sea. *Chin. J. Oceanol. Limnol.* 10 (2), 107–118.
- Wang, Z., Dong, S., Li, X., Soares, C.G., 2016. Assessments of wave energy in the Bohai sea, China. *Energy Rev.* 90, 145–156.
- Wang, Z., Zhou, L., Dong, S., Wu, L., Li, Z., Mou, L., Wang, A., 2014. Wind wave characteristics and engineering environment of the South China Sea. *J. Ocean Univ. China* 13 (6), 893–900.
- Zhang, D., Li, W., Lin, Y., 2009. Wave energy in China: current status and perspectives. *Energy Rev.* 34 (10), 2089–2092.
- Zheng, C.W., Pan, J., 2014. Assessment of the global ocean wind energy resource. *Renew. Sustain. Energy Rev.* 33 (50), 382–391.
- Zheng, C.W., Pan, J., Li, J.X., 2013. Assessing the China Sea wind energy and wave energy resources from 1988 to 2009. *Ocean Eng.* 65, 39–48.
- Zhu, L.S., Song, Y.F., Qiu, Z., Chen, X.H., Mai, B.Q., Qiu, Y.W., Song, L.L., 2003. Computation of wave, tide and wind currents for the south China sea under tropical cyclones. *China Ocean Eng.* 17 (4), 505–516.